Behavioral/Systems/Cognitive

Synaptic Currents in Anatomically Identified CA3 Neurons during Hippocampal Gamma Oscillations *In Vitro*

Iris Oren,[1] **Edward O. Mann,**[1] **Ole Paulsen,**[1] **and Norbert Hájos**[2]

[1]Department of Physiology, Anatomy, and Genetics, University of Oxford, Oxford OX1 3PT, United Kingdom, and [2]Department of Cellular and Network Neurobiology, Institute of Experimental Medicine, Hungarian Academy of Sciences, H-1450 Budapest, Hungary

Gamma-frequency oscillations are prominent during active network states in the hippocampus. An intrahippocampal gamma generator has been identified in the CA3 region. To better understand the synaptic mechanisms involved in gamma oscillogenesis, we recorded action potentials and synaptic currents in distinct types of anatomically identified CA3 neurons during carbachol-induced (20–25 μM) gamma oscillations in rat hippocampal slices. We wanted to compare and contrast the relationship between excitatory and inhibitory postsynaptic currents in pyramidal cells and perisomatic-targeting interneurons, cell types implicated in gamma oscillogenesis, as well as in other interneuron subtypes, and to relate synaptic currents to the firing properties of the cells. We found that phasic synaptic input differed between cell classes. Most strikingly, the dominant phasic input to pyramidal neurons was inhibitory, whereas phase-coupled perisomatic-targeting interneurons often received a strong phasic excitatory input. Differences in synaptic input could account for some of the differences in firing rate, action potential phase precision, and mean action potential phase angle, both between individual cells and between cell types. There was a strong positive correlation between the ratio of phasic synaptic excitation to inhibition and firing rate over all neurons and between the phase precision of excitation and action potentials in interneurons. Moreover, mean action potential phase angle correlated with the phase of the peak of the net-estimated synaptic reversal potential in all phase-coupled neurons. The data support a recurrent mechanism of gamma oscillations, whereby spike timing is controlled primarily by inhibition in pyramidal cells and by excitation in interneurons.

Key words: gamma oscillation; interneuron; synaptic; cholinergic; hippocampus; rat

Introduction

Gamma-frequency oscillations (30–100 Hz) are prevalent in active cortical networks. Although such network oscillations have been studied extensively *in vivo*, neither their underlying mechanisms nor functions are well understood (Paulsen and Sejnowski, 2006). In the hippocampal formation, gamma oscillations are often seen during theta activity (4–7 Hz), which occurs during exploratory behavior and rapid eye movement sleep (Buzsaki et al., 1983; Bragin et al., 1995; Csicsvari et al., 2003). Hippocampal gamma oscillations can also occur independently of theta oscillations (Penttonen et al., 1998; Csicsvari et al., 2003) and may be an inherent property of the local network.

In vitro models of gamma oscillations have provided some insights into the mechanisms of gamma oscillogenesis in the hippocampus. Analysis of carbachol (CCh)-induced gamma oscillations in hippocampal slices has identified an intrinsic gamma generator in area CA3 (Fisahn et al., 1998), which also appears to

operate *in vivo* (Csicsvari et al., 2003). The CA3 network architecture is highly recurrent (Amaral et al., 1990): pyramidal cells (PCs) innervate PCs and interneurons, which in turn synapse onto PCs and other interneurons, making recurrent feedback inhibition a strong candidate mechanism for the generation of gamma oscillations in CA3. A PC–interneuron recurrent model of CCh-induced oscillations is attractive because the same mechanism is suggested by the spike order of PCs and interneurons during theta-related gamma oscillations *in vivo* (Csicsvari et al., 2003), and theta activity itself is believed to depend on septal cholinergic input (Stewart and Fox, 1990). Other gamma models implicate an independent interneuronal network as the primary rhythm generator (Whittington et al., 1995; Whittington and Traub, 2003; Bacci and Huguenard, 2006; Vida et al., 2006).

To better understand the synaptic mechanisms involved in gamma oscillogenesis and to distinguish between these two models, the present study aimed to record synaptic currents in anatomically identified neurons during cholinergically induced gamma oscillations. If CCh-induced oscillations are generated by a recurrent mechanism, interneurons would be expected to receive a dominant phasic excitatory drive and PCs would be expected to receive a dominant phasic inhibitory input, whereas if oscillations result from an interneuronal network, the dominant phasic input to both PCs and interneurons should be inhibitory. We therefore wanted to compare and contrast the relationship between excitatory and inhibitory synaptic currents in PCs and

interneurons, focusing on PCs and perisomatic-targeting inter-neurons, cell types that have been suggested to underlie gamma oscillogenesis in the recurrent model (Fisahn et al., 1998; Gloveli et al., 2005a,b; Mann et al., 2005a,b). Furthermore, we wanted to relate the synaptic input to the firing properties of individual cells, which have been shown to differ between cell classes (Hájos et al., 2004). We found that synaptic input differed between cell classes and that differences in synaptic input could account for some of the differences in both the firing rate and phase coupling. Our results are consistent with a recurrent model for CCh-induced gamma oscillations in CA3.

Materials and Methods

Slice preparation. Experiments were conducted in accordance with the United Kingdom Animals (Scientific Procedures) Act (1986), the Hungarian Act of Animal Care and Experimentation (1998, XXVIII, section 243/1998), and the guidelines of the institutional ethical codes. Wistar rats (postnatal day 13–20) were deeply anesthetized with isoflurane and decapitated, and the brain was removed and placed in ice-cold cutting solution containing the following (in mM): 252 sucrose, 2.5 KCl, 26 NaHCO$_3$, 0.5 CaCl$_2$, 5 MgCl$_2$, 1.25 NaH$_2$PO$_4$, and 10 glucose. The cutting solution had been bubbled with 95% O$_2$/5% CO$_2$ (carbogen gas) for at least 30 min before use. Horizontal slices (350–400 μm thick) were cut and trimmed of most extrahippocampal areas. The slices were stored in interface conditions with artificial CSF (ACSF) containing the following (in mM): 126 NaCl, 3 KCl, 1.25 NaH$_2$PO$_4$, 2 MgSO$_4$, 2 CaCl$_2$, 26 NaHCO$_3$; and 10 glucose for at least 60 min before being transferred individually to the recording chamber.

Electrophysiological recordings. The recordings were conducted in a submerged-type recording chamber maintained at 29–33°C. Carbogen-bubbled ACSF was superfused at a flow rate of 3.5–5.5 ml/min. Oscillations were induced by bath application of 20–25 μM CCh (Sigma-Aldrich, St. Louis, MO). Patch pipettes ($\approx$4–8 MΩ) filled with ACSF were used to record field oscillations and action potentials extracellularly. The field pipette was placed in the stratum pyramidale of the CA3 region, whereas a second pipette was used to detect action potentials from individual neurons identified using differential interference contrast microscopy (Axioskop; Zeiss, Jena, Germany). Action potentials were recorded for ~60 s. The pipette was then withdrawn from the slice, and the cell was patched with a new pipette filled with intracellular solution containing the following: 138 mM K-gluconate, 3 mM CsCl, 10 mM phosphocreatine, 4 mM ATP, 0.4 mM GTP, 10 mM HEPES, 0.2 mM QX-314 [N-(2,6-dimethylphenylcarbamoylmethyl)-triethylammonium bromide], and 3 mg/ml biocytin. Seal resistance before whole-cell access was $\geq$1 GΩ. Whole-cell series resistance was in the range of 5–15 MΩ. All data were recorded with a Multiclamp 700A amplifier (Molecular Devices, Foster City, CA). During voltage-clamp recordings, series resistance compensation was applied as necessary using the built-in series resistance compensation of the amplifier (12–17 kHz, 40–75%). Voltage measurements were not corrected for liquid–liquid junction potential. To record EPSCs and avoid interference from inhibitory events, cells were voltage clamped at a nominal holding potential of the estimated reversal potential for IPSCs (−65 to −60 mV of the uncorrected potential). Similarly, IPSCs were recorded at a nominal holding potential of the estimated EPSC reversal potential (0–20 mV of the uncorrected potential). Both field and unit recordings were low-pass filtered at 2 kHz using the built-in Bessel filter of the amplifier. Data were digitized at 5 kHz with either a PCI-6042E board (National Instruments, Austin, TX) and EVAN 1.3 software (courtesy of Prof. I Mody, University of California, Los Angeles, CA) or an ITC-16 board (Instrutech, Port Washington, NY) and Igor software (Wavemetrics, Lake Oswego, OR). All data were analyzed off-line using Igor Pro 5.01.

Event detection and analysis. The field recording was further filtered using a digital, bidirectional, phase-conserving, low-pass filter at 1 kHz. Extracellular unit recordings were digitally, bidirectionally high-pass filtered at 40 Hz to isolate the spikes. Whole-cell recordings of postsynaptic currents (PSCs) were digitally, bidirectionally high-pass filtered at 1 Hz to filter out slow fluctuations in holding current. *Post hoc digital filtering*

was done using Igor DSP filters (ftp://ftp.wavemetrics.net/IgorPro/User_Contributions/DSPFilters.ipf.zip).

To measure the power of the field oscillation, power spectral density analysis was performed on recordings of ~60 s, using standard Igor Pro procedures. Time windows of ~1.5 s with 50% overlap were multiplied by a Hanning window to minimize end-effects before the fast Fourier transform was performed. Gamma power was taken as the area under the power spectral density curve between 20 and 40 Hz.

To examine phase coupling, event times were converted into phase with respect to the background field oscillation using wavelet analysis (Torrence and Compo, 1998; Le Van Quyen et al., 2001). The Morlet wavelet transform of the field recording was examined between 10 and 45 Hz with scales chosen to reflect the equivalent Fourier frequency (see Fig. 1C–E) (Torrence and Compo, 1998). For each time point, the maximum of the wavelet transform magnitude was found, and the corresponding frequency was identified. The phase of the time point was defined in terms of this dominant frequency (Fig. 1D,E). Phase was defined such that $-\pi$ was associated with the minimum of the oscillation, and a full cycle ran from $-\pi$ to π (see Fig. 1F). To validate the wavelet technique, a peak-to-peak linear mapping phase analysis of action potentials was also used. A significant positive correlation was found between action potential phase as determined by the two methods ($r = 0.83$; $p < 0.01$; $n = 35$; angular–angular correlation; data not shown).

Phasic charge transfer was calculated as the mean of the integral from a baseline value over each cycle with the baseline defined as follows: (1) an overall initial baseline level estimate was obtained by computing the cycle-averaged event for the entire recording (see below). The maximum (for EPSCs) or minimum (for IPSCs) of this average event was taken as the initial baseline estimate. (2) For each 0.2 s epoch, the mean of all current values exceeding this initial baseline estimate was calculated. This mean was used as the baseline for the epoch. (3) If no current value was found to exceed the initial baseline estimate during the epoch, the baseline estimate would increment negatively for EPSCs and positively for IPSCs until such current values were found. This was repeated for all epochs of the entire recording (see Fig. 2B,C). Event times for PSCs were defined as time of peak current per cycle of the oscillation, and these were converted to wavelet phases as described.

The cycle-averaged field and cycle-averaged events (see Figs. 1G, 3B) were obtained by summing recordings over cycles between $-\pi$ and π and dividing by the number of cycles. Cycles were scaled to span 2π radians. This phase is referred to as the cycle-averaged phase to distinguish it from the phase as defined by wavelet analysis.

The net apparent reversal potential (E_{syn}^{rev}) was estimated by first converting the cycle-averaged PSCs to excitatory (g_e) and inhibitory (g_i) conductances using the following equation:

$$g_{e/i} = \frac{I_{e/i}}{(V_h - E_{e/i}^{rev})}, \tag{1}$$

where $I_{e/i}$ is the phasic excitatory/inhibitory current, V_h is the holding potential, and $E_{e/i}^{rev}$ is the estimated reversal potential for the conductance of interest. The conductances were used to estimate the membrane potential of zero synaptic current (E_{syn}^{rev}) by solving the following equation:

$$I_{syn} = g_e(E_{syn}^{rev} - E_e^{rev}) + g_i(E_{syn}^{rev} - E_i^{rev}) = 0 \tag{2}$$

$$\Rightarrow E_{syn}^{rev} = \frac{I_{syn} + g_e E_e^{rev} + g_i E_i^{rev}}{g_e + g_i}.$$

Event times for action potentials were defined as the time of crossing a voltage threshold set by visual inspection, and the event phase was taken as the wavelet phase of the dominant frequency at this event time. Analysis was done both by using all spikes per cycle and only the first spike per cycle. A significant positive correlation for phase-coupling variables (see below, Statistics) was found between values obtained with the two methods (action potential coupling strength: $r = 0.99$, $p < 0.01$, $n = 43$, Pearson's correlation; mean action potential phase: $r = 0.99$, $p < 0.01$, $n = 35$, angular–angular correlation; data not shown). The results reported here use all events detected.

To evaluate spike-timing precision, spike times (Δt_i) were defined as

the time difference between the preceding minimum of the smoothed field oscillation and the time of threshold crossing. If $\Delta t_I \geq T_i/2$, where T_i is the cycle period, then Δt_i was taken as the negative time difference from the subsequent minimum. T_i was calculated as the time between two consecutive minima in the field oscillation (see Fig. 4A). To enable comparison between the SDs for spike times ($\sigma_{\Delta t}$) and the corresponding SD for phase (σ_ϕ), $\sigma_{\Delta t}$ was normalized by the cycle period as follows:

$$\sigma_t^{norm} = \frac{\sigma_{\Delta t}}{\bar{T}}, \tag{3}$$

where $\bar{T}$ is the mean oscillation period. This quantity is comparable to the normalized SD of phase:

$$\sigma_\phi^{norm} = \frac{\sigma_\phi}{2\pi}, \tag{4}$$

where σ_ϕ is taken as the circular SD (see below, Statistics).

In some slices, phase-coupling strength of action potentials varied over time with the oscillation power such that phase-coupling strength decreased with decreasing oscillation magnitude (data not shown). Therefore, a reduced data set was obtained for the analysis of the relationships between synaptic events and firing properties. Cells for which the wavelet magnitude of the field oscillation changed by >2 SDs between spike train and PSC recordings were excluded from the reduced data set. Results are stated for both the full and reduced data set where applicable.

Statistics. Coefficients of variation of the magnitude and frequency of the field oscillation (CV_{mag} and CV_{freq}, respectively) were calculated from the SD of the maximum magnitude and the SD of the corresponding dominant frequency of the wavelet transform for each time point over the entire recording.

Circular statistics were used to determine the phase coupling of events. The phase of each event was represented by a unit vector pointing in the direction of the phase angle. The individual vectors were summed vectorially over the time epoch in question to give a resultant vector, $\vec{R}$. The direction of the resultant vector, ϕ, was used as the mean event phase for the epoch. The normalized length of $\vec{R}$, $r = |\vec{R}|/n$, where n is the number of events, served as a measure of the strength of the phase coupling. If the events are perfectly phase coupled, $r = 1$. If events are random, the vectors will cancel, and $r \to 0$.

To determine the significance of the phase coupling, the Rayleigh probability of $\vec{R}$ was calculated using the following:

$$p = e^{-z} \times \left(1 + \frac{2Z - Z^2}{4n} - \frac{24Z - 132Z^2 + 76Z^3 - 9Z^4}{288n^2} \right), \tag{5}$$

where n is the number of spikes, and $Z = n\,r^2$ (Fisher, 1993).

Before testing equality of means of linear variables, the Levene statistic was evaluated to test homogeneity of variances. ANOVA was used to compare means between homogenous distributions ($p > 0.05$, Levene statistic), and the more robust Welch statistic was used for non-homogenous distributions. The Bonferroni *post hoc* test was performed to find significant differences between distributions with equal variance. The Games-Howell *post hoc* test was performed to find significant differences between distributions with unequal variances. The multi-sample Watson-Williams test (Zar, 1999) was used to test equality of means of angular variables. The tests used in each case are specified in the text.

Before correlation tests for linear variables, the normality of a distribution was tested by the Kolmogorov–Smirnov test. To correlate variables from normal distributions ($p > 0.05$, Kolmogorov–Smirnov test), the Pearson's correlation coefficient was used. For variables from non-normal distributions, the more robust Spearman's rank correlation coefficient was used.

To correlate angular–angular variables, the following parametric angular–angular correlation coefficient was used:

$$r = \frac{\displaystyle\sum_{i=1}^{n-1} \sum_{j=i+1}^{n} \sin(a_i - a_j)\sin(b_i - b_j)}{\sqrt{\displaystyle\sum_{i=1}^{n-1} \sum_{j=i+1}^{n} \sin^2(a_i - a_j) \sum_{i=1}^{n-1} \sum_{j=i+1}^{n} \sin^2(b_i - b_j)}}, \tag{6}$$

where the ith pair of data are denoted as a_i, b_i. The confidence interval was determined by a jackknifing procedure (Zar, 1999). All correlation coefficients are quoted as r, and tests used are specified in the text.

The circular SD was taken as follows:

$$\sigma = \sqrt{-2 \ln r}, \tag{7}$$

where r is the phase-coupling strength (Zar, 1999). Values are given as mean $\pm$ SEM, unless stated otherwise.

Anatomical identification. After intracellular recording and biocytin filling, the slice was fixed in 4% paraformaldehyde in 0.1 M phosphate buffer (PB), pH 7.4, for at least 30 min, followed by washout with PB several times and incubation in cryoprotecting solution (30% sucrose in 0.01 M PB) for 2 h. Slices were then freeze-thawed three times above liquid nitrogen and treated with 1% H_2O_2 in PB for 15 min to reduce endogenous peroxidase activity. Filled cells were visualized using avidin-biotinylated horseradish peroxidase complex reaction (Vector Laboratories, Burlingame, CA) with nickel-intensified 3,3'-diaminobenzidine (Sigma-Aldrich, St. Louis, MO) as chromogen giving a dark reaction product. After dehydration and embedding in Durcupan (Sigma-Aldrich), neurons were identified based on their dendritic and axonal arborization, and representative cells were reconstructed with the aid of a drawing tube using a 40× objective (see Fig. 2).

Results

Fast network oscillations were induced in the CA3 region of horizontal hippocampal slices by bath application of CCh (20–25 μM). The network oscillations were monitored by recording the field potential using an ACSF-filled micropipette placed in the stratum pyramidale. Action potentials of individual neurons were recorded extracellularly from visually selected neurons using a second ACSF-filled pipette. This second pipette was then withdrawn, and the EPSCs and IPSCs were recorded in whole-cell voltage-clamp mode with a pipette containing intracellular solution. Biocytin in the intracellular solution was used for *post hoc* anatomical identification of recorded cells. Of 74 neurons, 43 cells were successfully recovered and anatomically identified based on their dendritic and axonal arborization. Only anatomically identified neurons were included in the following analysis. Data reported excludes outliers (defined as >3 SDs from the mean of the measure of interest for each cell type). Two cells were excluded from additional analysis on this basis.

CCh-induced fast network oscillations

To characterize the field oscillations, extracellular recordings of ~1 min (Fig. 1A) were acquired and used to obtain a power spectrum (Fig. 1B). Calculation of the power spectral density function revealed a peak in the beta–gamma frequency range with a mean peak frequency over all recordings of 28.1 ± 0.6 Hz (f_{PSD}) and mean gamma power of 1782.9 ± 418.7 μV^2 ($n = 43$). Wavelet analysis using a Morlet wavelet basis (Fig. 1C) was used to extract the magnitude and phase of different frequency components (10–45 Hz) of the field oscillation (Fig. 1D–F). Both the maximum field wavelet magnitude and the corresponding dominant wavelet frequency fluctuated over time ($CV_{mag} = 24.4 \pm 1.1\%$; $CV_{freq} = 14.1 \pm 1.2\%$; see Materials and Methods). Inspec-

tion of Figure 1, *A* and *D*, suggests that the fluctuations in the oscillation magnitude might be rhythmical. Indeed, in 28 of the 43 recordings, a power spectrum analysis of the maximum wavelet magnitude over time revealed a low frequency peak (2.8 ± 1.6 Hz; $n = 28$; data not shown).

To further validate that wavelet analysis provided an appropriate definition of phase, the cycle-averaged field potential was calculated (Fig. 1*G*) (see Materials and Methods). This had a regular form, providing qualitative support for the method. Moreover, the frequency corresponding to the period of these cycle-averaged events (29.6 ± 0.7 Hz; $n = 43$) was similar to and correlated with f_{PSD} ($r = 0.95$; $p < 0.01$, Pearson's correlation; $n = 43$).

Comparison of synaptic input in different cell types

To understand the synaptic mechanisms underlying gamma oscillations, PSCs were recorded from PCs (Fig. 2*Ai*) ($n = 17$) and perisomatic-targeting interneurons (basket and axo-axonic cells; $n = 9$) (Fig. 2*Aii*). Recordings were also obtained from dendritic-targeting interneurons [$n = 7$, comprising OLM cells, interneurons with a dendritic tree in the stratum oriens projecting to the stratum lacunosum moleculare ($n = 3$), and radiatum cells/radiatum-lacunosum-moleculare cells ($n = 4$)] (Fig. 2*Aiii*) and interneuron-selective interneurons [as defined by Hájos et al. (2004); $n = 7$] (Fig. 2*Aiv*) for comparison. Cells were voltage clamped at the estimated inhibitory and excitatory reversal potentials to record EPSCs and IPSCs, respectively (Fig. 2*B,C*) (see Materials and Methods). This information could reveal differences in the dominant input to cells and thus suggest a functional network architecture underlying gamma oscillations. Hereafter, any reference to excitation or inhibition refers to phasic excitation or phasic inhibition.

If phasic excitation drives cell firing, differences in the excitatory input to the cells may lead to differences in the recruitment of the various subpopulations of neurons. Phasic excitatory charge transfer (Q_e) differed significantly between cell types (Fig. 2*D*) ($p < 0.01$, Welch statistic; $n = 40$). Q_e was smallest in PCs ($Q_e = 0.56 \pm 0.063$ pC; $n = 17$) and was, on average, largest in perisomatic-targeting interneurons ($Q_e = 3.1 \pm 0.91$ pC, $n = 9$; dendritic-targeting interneurons: $Q_e = 0.94 \pm 0.267$ pC, $n = 7$; interneuron-selective interneurons: $Q_e = 2.2 \pm 0.42$ pC, $n = 7$).

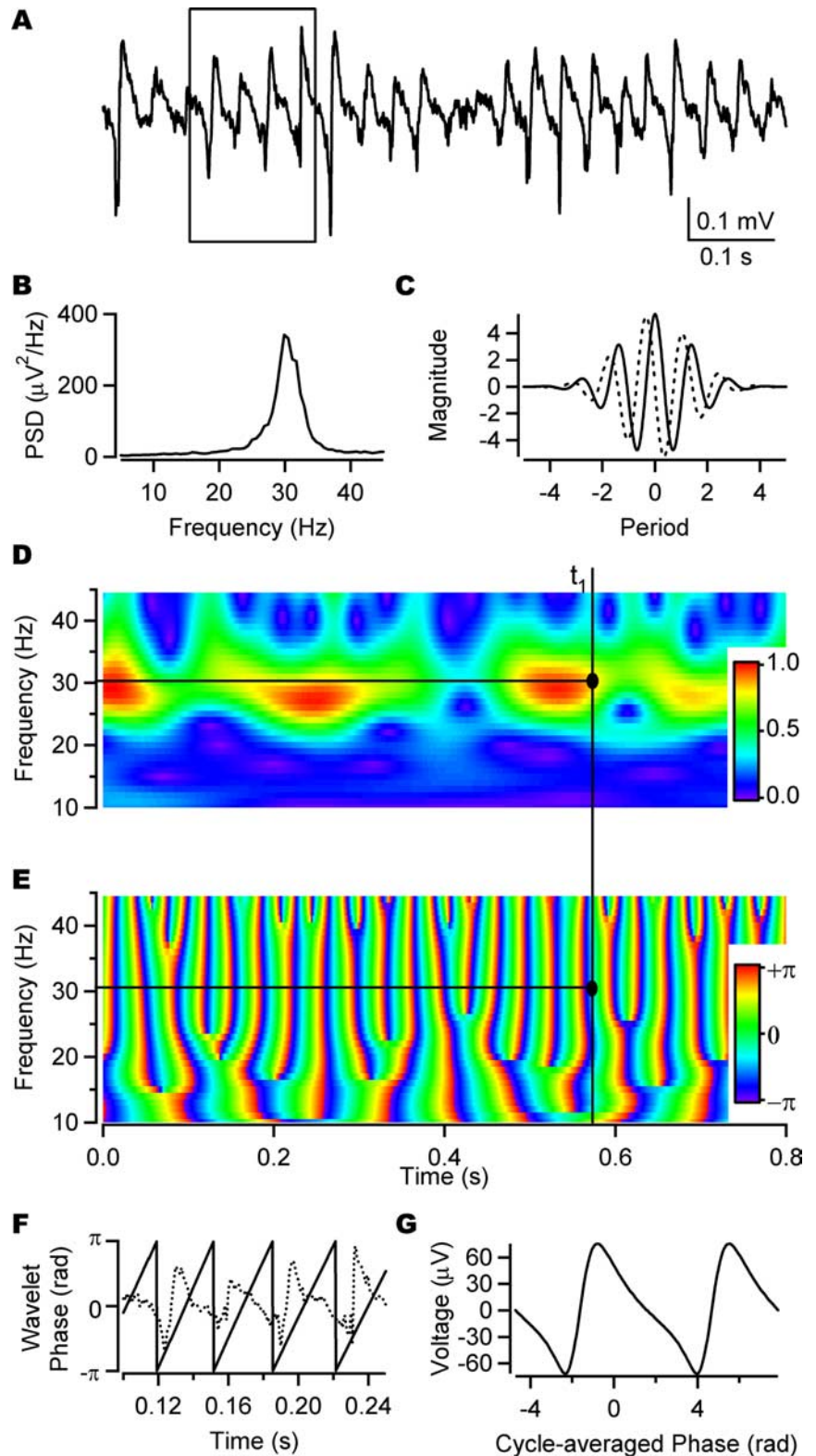The balance of excitation and inhibition was investigated by comparison of the

Figure 1. Wavelet analysis of CCh-induced field oscillation. ***A***, Field oscillation recorded extracellularly from the stratum pyramidale of the CA3 region after bath application of 20 μ_M CCh. ***B***, Power spectral density function of the trace in ***A*** showing gamma-frequency peak. ***C***, Real component (solid) and imaginary component (dotted) of Morlet wavelet basis. ***D***, Normalized magnitude component of wavelet transform of the trace in ***A***. ***E***, Phase component of wavelet transform of the trace in ***A***. ***D*** and ***E*** show how the phase of the gamma oscillation is defined for an arbitrary time, t_1. The dominant frequency at t_1 is defined as the frequency of the maximum magnitude at time t_1 (here ∼30 Hz). The oscillation phase is then determined for the dominant frequency at time t_1. The time scale is the same for ***A***, ***D***, and ***E***. ***F***, Expansion of the boxed area in ***A*** showing phase for all time points as defined by the dominant frequency of the wavelet transform as shown in ***D*** and ***E***. ***G***, Cycle average of the field oscillation in ***A***, with the start of each cycle defined by the wavelet phase.
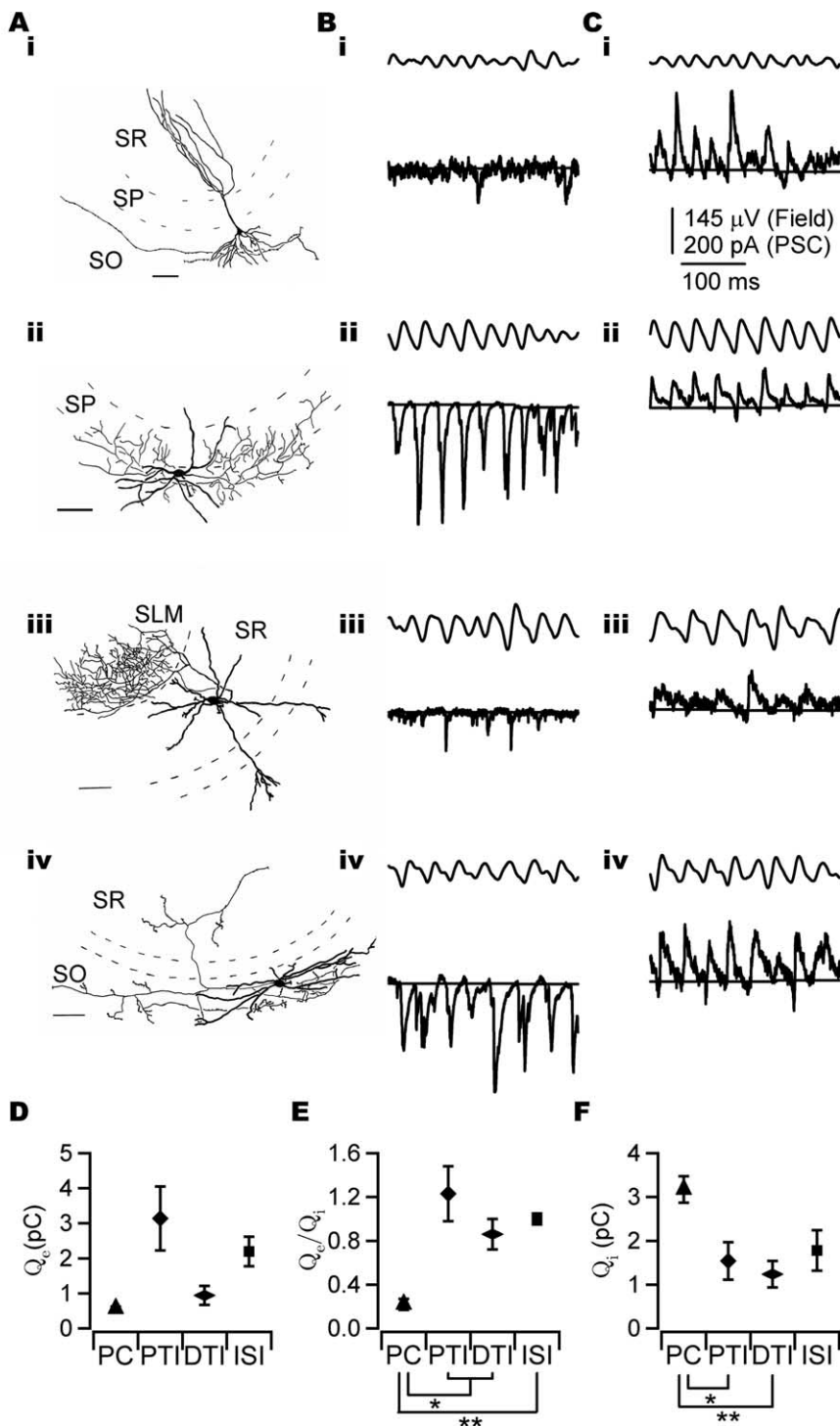
Figure 2. Phasic charge transfer of EPSCs and IPSCs during CCh-induced oscillations. *A*, Camera lucida drawing of a PC (*i*), perisomatic-targeting interneuron (a putative axo-axonic cell; *ii*), dendritic-targeting interneuron (radiatum-lacunosum moleculare cell; *iii*), and interneuron-selective interneuron (*iv*). SR, Stratum radiatum; SP, stratum pyramidale; SO, stratum oriens; SLM, stratum lacunosum-moleculare. *B*, Bidirectional bandpass-filtered field potential (10 – 45 Hz; top trace) and EPSCs (bottom trace) recorded from the soma of the cells illustrated in *A*, at a holding potential of −60 mV. *C*, Bidirectional bandpass-filtered field potential (10 – 45 Hz; top trace) and IPSCs (bottom trace) recorded from the same cells at 0 mV (*i*), +20 mV (*ii*), and +10 mV (*iii*, *iv*). The horizontal solid line is the calculated baseline used for phasic charge estimation (see Materials and Methods). *D*, The phasic excitatory charge (Q_e) differed significantly between cell classes ($p < 0.01$). PCs, $n = 17$; perisomatic-targeting interneurons, $n = 9$; dendritic-targeting interneurons, $n = 7$; interneuron-selective interneurons, $n = 7$. *E*, Phasic excitatory to inhibitory charge ratio (Q_e/Q_i) in different cell classes. Q_e/Q_i was smaller in PCs than in all classes of interneuron. PCs, $n = 17$; perisomatic-targeting interneurons, $n = 7$; dendritic-targeting interneurons, $n = 7$; interneuron-selective interneurons, $n = 4$. *F*, PCs received a significantly larger phasic inhibitory charge (Q_i) than perisomatic-targeting interneurons and dendritic-targeting interneurons. The number of cells is as in *E*. Error bars indicate SEM. *$p < 0.05$; **$p < 0.01$. Scale bars, 100 μm. PTI, Perisomatic-targeting interneuron; DTI, dendritic-targeting interneuron; ISI, interneuron-selective interneuron.

ratio of phasic excitatory to inhibitory charge (Q_e/Q_i) between cell types. Phasic inhibition exceeded phasic excitation in all PCs ($Q_e/Q_i = 0.23 \pm 0.049$; $n = 17$), whereas the dominant input to interneurons was often excitatory with perisomatic-targeting interneurons showing the largest excitation to inhibition ratio ($Q_e/Q_i = 1.2 \pm 0.25$, $n = 7$; dendritic-targeting interneurons: $Q_e/Q_i = 0.86 \pm 0.14$, $n = 7$; interneuron-selective interneurons: $Q_e/Q_i = 1.0 \pm 0.05$, $n = 4$) (Fig. 2E). The difference in Q_e/Q_i between PCs and interneuron classes was significant (Fig. 2E) ($p < 0.01$, Welch statistic and ANOVA with *post hoc* Games-Howell test; $n = 35$).

Although the significant difference in Q_e/Q_i between PCs and interneurons could result from a larger phasic excitatory input to interneurons, a larger phasic inhibitory input to PCs could also contribute to this difference. Comparison of Q_i between cell types revealed a significantly larger Q_i in PCs ($Q_i = 3.2 \pm 0.30$ pC; $n = 17$) than in interneurons (Fig. 2F) ($n = 35$; $p < 0.01$, ANOVA; perisomatic-targeting interneurons: $Q_i = 1.5 \pm 0.43$ pC, $n = 7$; dendritic-targeting interneurons: $Q_i = 1.2 \pm 0.30$ pC, $n = 7$; interneuron-selective interneurons: $Q_i = 1.8 \pm 0.46$ pC, $n = 4$). Interestingly, Q_i was found to correlate with field magnitude ($r = 0.58$; $p < 0.01$, Pearson's correlation; $n = 35$) (see supplemental Fig. 1, available at www.jneurosci.org as supplemental material), and this might account for some of the observed difference in Q_i between cell type ($p < 0.05$, ANOVA with field magnitude as covariate; $n = 35$; partial $\eta^2_{\text{celltype}} = 0.25$; partial $\eta^2_{\text{fieldmag}} = 0.16$). A correlation between charge and field magnitude was not seen for excitatory charge ($r = -0.21$; $p = 0.80$, Spearman's correlation; $n = 40$) (see supplemental Fig. 1, available at www.jneurosci.org as supplemental material). The data support the conclusion that both excitatory and inhibitory inputs differ between cell types.

The majority of cells received significantly phase-coupled ($p < 0.05$, Rayleigh probability) excitatory and inhibitory synaptic input as measured by the phase of the peak current recorded in each cycle (40 of 40 and 36 of 37, respectively). The coupling strength of the peak of the EPSC (r_e) did not differ significantly between cell types (Fig. 3Ai) ($p = 0.27$, ANOVA; $n = 40$), whereas the coupling strength of inhibitory inputs (r_i) was significantly larger in PCs ($r_i = 0.83 \pm 0.024$; $n = 17$) than in interneurons (Fig. 3Aii) ($p < 0.01$, Welch statistic; $n = 37$; perisomatic-targeting

interneurons: $r_i = 0.63 \pm 0.074$, $n = 9$; dendritic-targeting interneurons: $r_i = 0.46 \pm 0.122$, $n = 7$; interneuron-selective interneurons: $r_i = 0.57 \pm 0.059$, $n = 4$).

In all cells, the phase of the peak of the cycle-averaged EPSC preceded the peak of the cycle-averaged IPSC (Fig. 3B). To capture the temporal interaction between inhibitory and excitatory synaptic conductances, the effective synaptic conductance was estimated by calculation of the net apparent synaptic reversal potential E_{syn}^{rev} (see Materials and Methods). The shape of the E_{syn}^{rev} curve differed between PCs and interneurons (Fig. 3C), with the half-width (measured in radians) of the peak of the E_{syn}^{rev} curve being significantly narrower in PCs (half-width of 0.79 ± 0.157; $n = 17$) than in interneurons (Fig. 3D) ($p < 0.01$, ANOVA with Bonferroni *post hoc* test; $n = 35$; perisomatic-targeting interneurons: half-width of 2.6 ± 0.32, $n = 7$; dendritic-targeting interneurons: half-width of 2.6 ± 0.25, $n = 7$; interneuron-selective interneurons: half-width of 2.7 ± 0.23, $n = 4$), primarily as a result of the dominant inhibitory input received by PCs.

Firing properties of anatomically identified neurons during fast network oscillations

To characterize the firing properties of the cells, action potentials were recorded extracellularly for ~1 min (Fig. 4A) before whole-cell recording with another pipette (see Materials and Methods for details). The firing properties of the cells were quantified using three parameters: mean firing rate, action potential coupling strength (r_{AP}), and mean action potential phase (ϕ_{AP}; see Materials and Methods).

Firing rate
PCs fired at a significantly lower rate (6.0 ± 0.82 Hz; $n = 17$) than interneurons (Fig. 4B) ($p < 0.01$, Welch statistic and ANOVA with Games-Howell *post hoc* test; $n = 42$), whereas perisomatic-targeting (rate, 19 ± 2.3 Hz; $n = 10$) and interneuron-selective (rate, 21 ± 3.2 Hz; $n = 8$) interneurons fired at slightly higher rates than dendritic-targeting interneurons (rate, 16 ± 2.8 Hz; $n = 7$), in agreement with previous results (Hájos et al., 2004).

Phase versus time
The timing of action potentials after synaptic excitation may be the result of the intrinsic properties of the neuron, recurrent inhibitory synaptic input from the network, or both. If intrinsic properties play a dominant role in governing spike timing, then the absolute spike time after
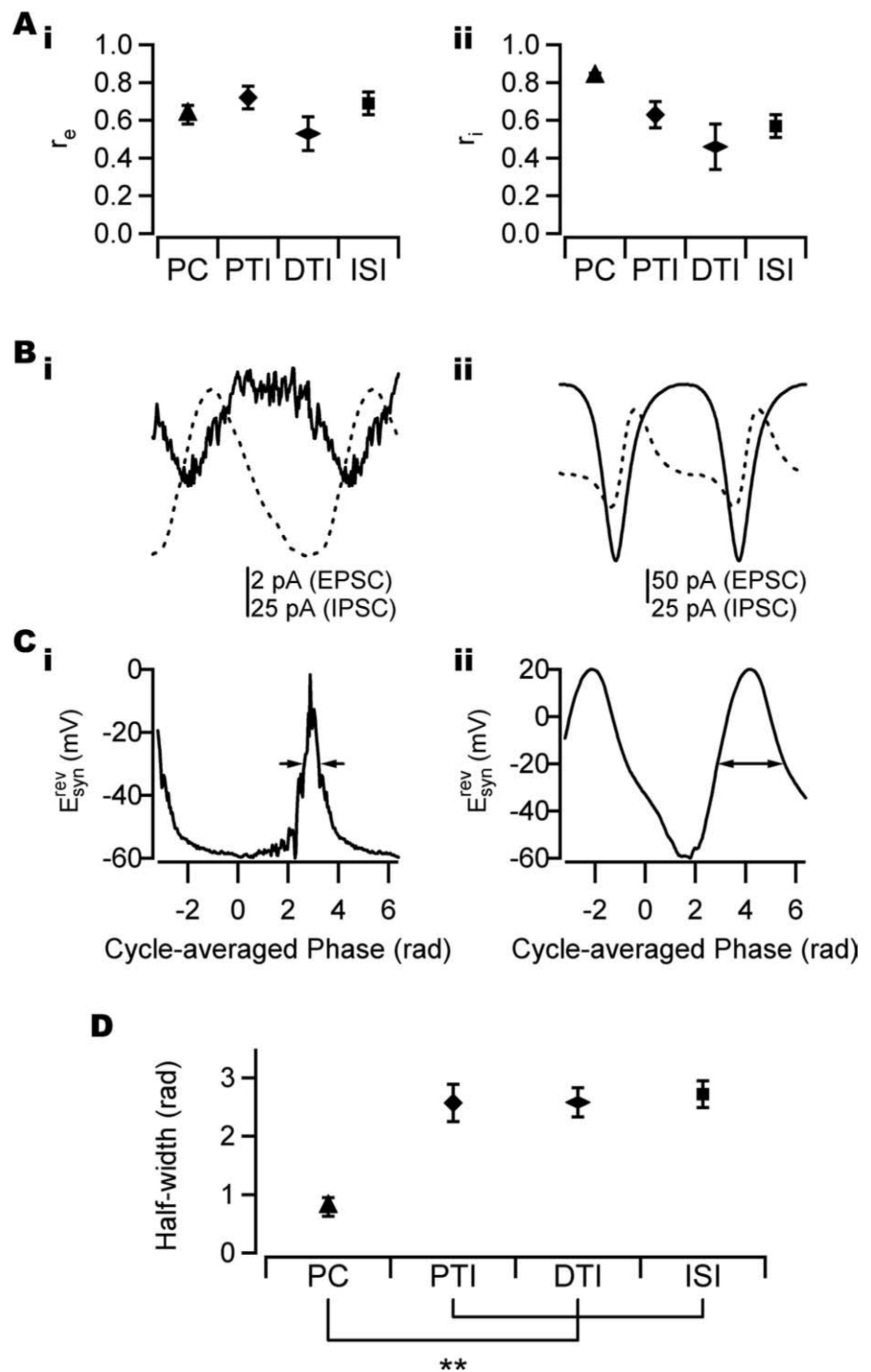

Figure 3. PSC phase-coupling strength and synaptic reversal potential during CCh-induced oscillations. **A**, Coupling strength of PSCs as measured by the phase of the peak time in different cell types. **i**, No significant difference was seen in EPSC coupling strength (r_e) between cell types. PCs, $n = 17$; perisomatic-targeting interneurons, $n = 9$; dendritic-targeting interneurons, $n = 7$; interneuron-selective interneurons, $n = 7$. **ii**, A significant difference in IPSC coupling strength (r_i) was found between cell types ($p < 0.01$). PCs, $n = 17$; perisomatic-targeting interneurons, $n = 9$; dendritic-targeting interneurons, $n = 7$; interneuron-selective interneurons, $n = 4$. **B**, Cycle-averaged PSCs in PC (**i**) and perisomatic-targeting interneuron (**ii**). Solid line, EPSC; dotted line, IPSC. The same cells as in Figure 2, *Ai* and *Aii*, are shown. Note the different scales in **i** and **ii**. **C**, Net apparent synaptic reversal potential (E_{syn}^{rev}) for cells in **B**. For details of calculation, see Materials and Methods. Arrows indicate half-width of E_{syn}^{rev}. **D**, Half-width of E_{syn}^{rev} in different cell classes. The difference in half-width of E_{syn}^{rev} between PCs and interneurons was significant (**$p < 0.01$). PCs, $n = 17$; perisomatic-targeting interneurons, $n = 7$; dendritic-targeting interneurons, $n = 7$; interneuron-selective interneuron, $n = 4$. Error bars indicate SEM. PTI, Perisomatic-targeting interneuron; DTI, dendritic-targeting interneuron; ISI, interneuron-selective interneuron.

A

B

C

D

E

F
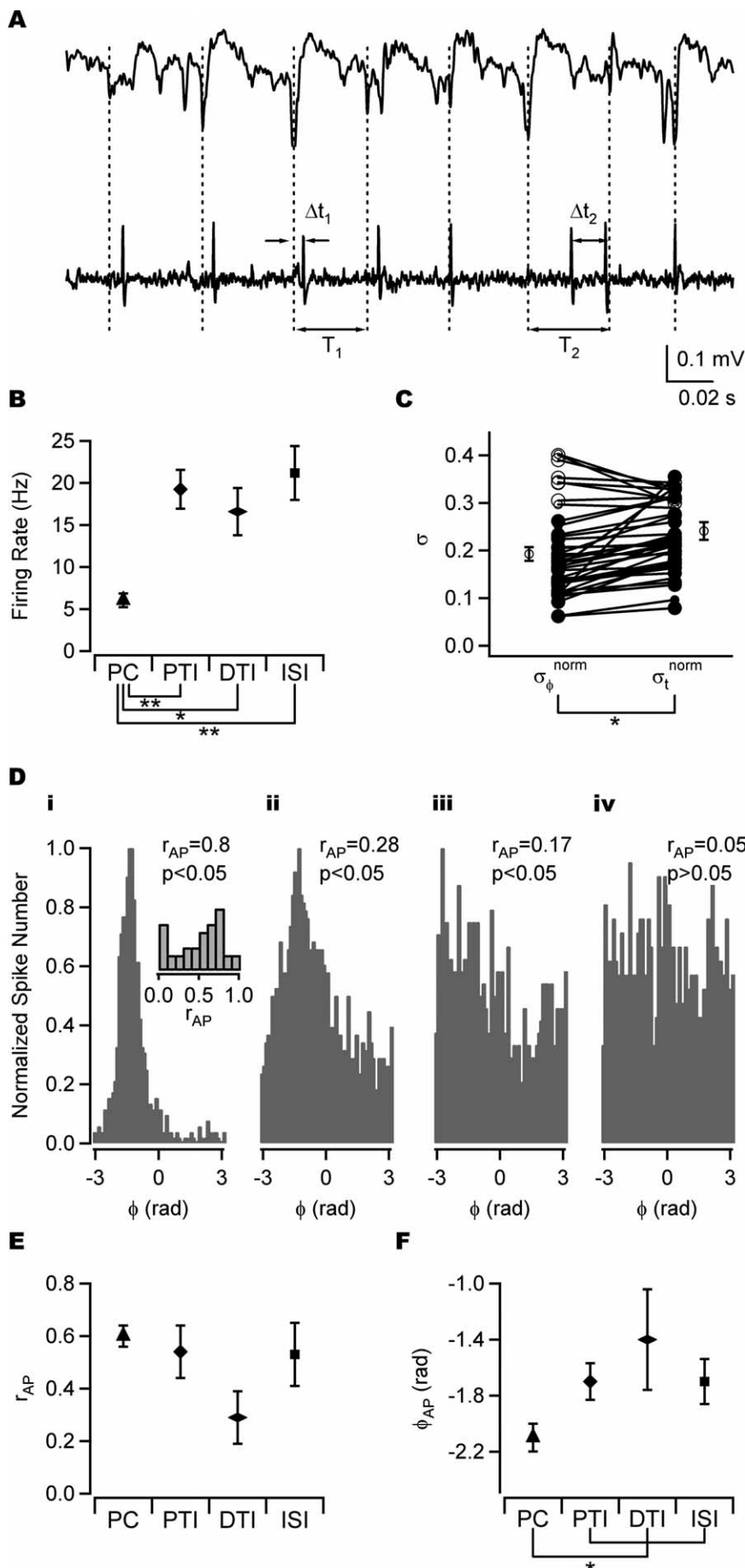
the arrival of the excitatory synaptic input should remain constant independent of the oscillation frequency. Alternatively, spike timing might be more tightly controlled by both the excitatory and inhibitory synaptic input. The field oscillation emerges from the total network activity, and therefore if spike timing is predominantly controlled by both the excitatory and inhibitory synaptic input, variability in spike phase relative to the field oscillation should be smaller than variability in absolute time. This provided the motivation to compare spike-timing precision in terms of absolute time and phase. If the oscillation frequency remains constant, the two measures should give comparable results. However, if the frequency varies over the recording, the results will differ. The SD of spike times relative to the field oscillation (σ_t^{norm}) and the SD of the spike phases (σ_ϕ^{norm}; see Materials and Methods) were used to evaluate precision (Mainen and Sejnowski, 1995). Overall, σ_ϕ^{norm} was significantly smaller than σ_t^{norm} (Fig. 4C) ($p < 0.05$, paired-samples t test; $n = 42$), indicating that both excitatory and inhibitory synaptic inputs are important in the control of spike timing of CA3 neurons. However, $\sigma_t^{norm} > \sigma_\phi^{norm}$ in cells that were weakly phase coupled ($r_{AP} < 0.2$; see below, Action potential phase-coupling strength).

←

Figure 4. Firing properties of distinct types of neuron during CCh-induced oscillations. **A**, Simultaneous extracellular recordings of field potential (top trace) and spike train (bottom trace) from an anatomically identified perisomatic-targeting interneuron. ΔT_i, Relative spike times used for time analysis of precision; T_i, cycle periods used for time analysis of precision (see Materials and Methods). **B**, Firing rate in different cell classes. PCs ($n = 17$) fired at significantly lower rates than perisomatic-targeting interneurons ($n = 10$), interneuron-selective interneurons ($n = 8$), and dendritic-targeting interneurons ($n = 7$). **C**, Comparison of phase and time precision as quantified by the SD of phase normalized by 2π (σ_ϕ^{norm}) and SD of time relative to oscillation minimum normalized by the mean oscillation period (σ_t^{norm}). σ_ϕ^{norm} was significantly smaller than σ_t^{norm}. **D**, Spike-phase histograms normalized by the maximum bin count of strongly phase-coupled cells (**i, ii**), weakly phase-coupled cell (**iii**), and non-phase-coupled cell (**iv**). Inset, Histogram of action potential phase-coupling strength (r_{AP}) over all cells showing a bimodal distribution with minimum around $r_{AP} = 0.2$, the cutoff value between strong and weak phase coupling. **E**, Average r_{AP} in different cell types. The number of cells is as in **B**. **F**, Firing phase (ϕ_{AP}) of strongly phase-coupled cells in different cell types. PCs fired significantly earlier than all classes of interneurons. PCs, $n = 17$; perisomatic-targeting interneurons, $n = 8$; dendritic-targeting interneurons, $n = 3$; interneuron-selective interneurons, $n = 6$. Error bars indicate SEM. *$p < 0.05$; **$p < 0.01$. PTI, Perisomatic-targeting interneuron; DTI, dendritic-targeting interneuron; ISI, interneuron-selective interneuron.

Action potential phase-coupling strength
Thirty-eight of the 42 cells were significantly phase coupled ($p <$ 0.05, Rayleigh probability). The degree of phase coupling varied between significantly phase-coupled cells. The distribution of r_{AP} appeared bimodal with a minimum around $r_{AP} = 0.2$ (Fig. 4D, inset). This was set as the cutoff value to classify cells as strongly or weakly phase coupled. Inspection of the spike-phase histograms confirmed this as an appropriate choice (Fig. 4D) [see also Hájos et al. (2004), their Fig. 7C]. The phase histogram of strongly phase-coupled cells ($r_{AP} > 0.2$) exhibited a clear peak in the phase histogram, whereas the phase histograms of weakly phase-coupled cells did not. The majority of PCs, perisomatic-targeting, and interneuron-selective interneurons were strongly phase coupled ($r_{AP} > 0.2$; 17 of 17, 8 of 10, and 6 of 8, respectively), whereas this was the case for only 3 of the 7 dendritic-targeting interneurons (Fig. 4D). It has been reported that the precision of phase coupling is lower in PCs than in the majority of interneurons (Hájos et al., 2004). Consistent with this, r_{AP} of PCs tended to be smaller than that of strongly coupled perisomatic-targeting interneurons (0.60 ± 0.04, $n = 17$ vs 0.66 ± 0.08, $n = 8$). Action potential phase-coupling strength was, on average, weakest in dendritic-targeting interneurons, consistent with previous findings (Hájos et al., 2004). The difference in r_{AP} between cell types failed to reach statistical significance (Fig. 4E) ($p = 0.1$, Welch statistic; $n = 42$).

Mean action potential phase angle
Strongly phase-coupled PCs fired near the minimum of the field oscillation ($\phi_{AP} = -2.1 \pm 0.09$; $n = 17$; phase measured in radians), whereas strongly phase-coupled interneurons tended to fire later in the cycle. This difference was significant (Fig. 4F) ($p < 0.01$, Watson-Williams test; $n = 34$). Phase-coupled dendritic-targeting interneurons tended to fire later in the cycle ($\phi_{AP} = -1.4 \pm 0.36$; $n = 3$) than perisomatic-targeting ($\phi_{AP} = -1.7 \pm 0.13$; $n = 8$) and interneuron-selective ($\phi_{AP} = -1.7 \pm 0.16$; $n = 6$) interneurons, but this was not statistically significant (Fig. 4F) ($p = 0.20$ and $p = 0.34$, respectively, Watson-Williams test). These findings are consistent with the findings of Hájos et al. (2004).

Thus, different cell types display different firing properties during CCh-induced oscillations with respect to firing rate, action potential coupling strength, and mean action potential phase angle.

Synaptic input and firing properties during fast network oscillations
The relationship between synaptic input from the network and firing properties was investigated next in terms of the three parameters discussed, namely firing rate, action potential phase-coupling strength, and mean action potential phase angle.

Synaptic input and firing rate
If phasic excitatory input drives cells to fire, the firing rate would be expected to vary with the magnitude of the excitatory input. Hence, the relationship between Q_e and spike rate was investigated. Over all cells, a significant positive correlation was found between rate and excitatory charge (Fig. 5A) (full set: $r = 0.51$, $p < 0.01$, $n = 39$; reduced set: $r = 0.61$, $p < 0.01$, $n = 31$; Spearman's correlation; see Materials and Methods). We have shown that perisomatic-targeting and interneuron-selective interneurons fire at a higher rate than PCs and dendritic-targeting cells (Fig. 4B). If the firing rate is controlled by excitatory synaptic input, perhaps differences in the amount of excitation received by different cell classes could account for differences in the firing rate.
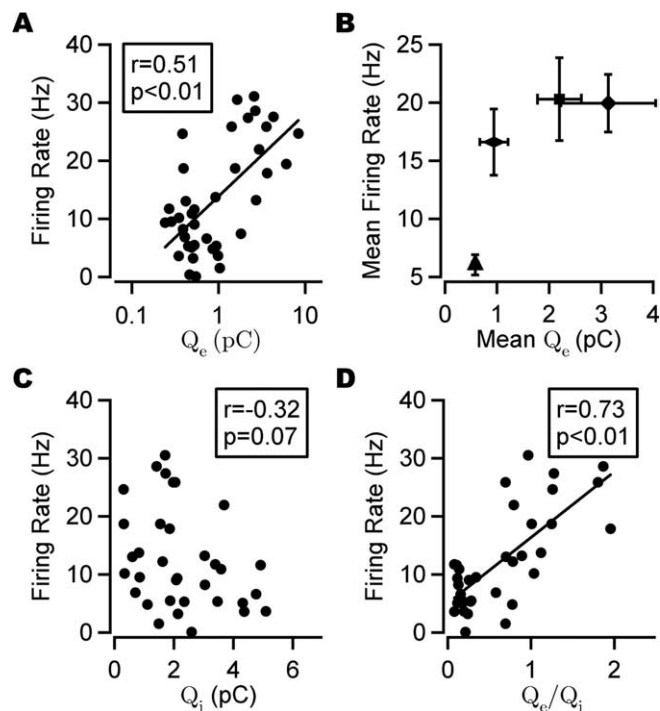

Figure 5. Firing rate and phasic synaptic charge transfer. *A*, Firing rate plotted against phasic excitatory charge transfer (Q_e) for individual cells. Overall, a significant correlation (Spearman's correlation) was found between the firing rate and Q_e (shown here on a log scale). A least-square fit line is shown. *B*, Relationship between the firing rate and Q_e in different cell classes. Both the mean firing rate and Q_e were higher, on average, in perisomatic-targeting interneurons ($n = 9$) and interneuron-selective interneurons ($n = 7$) compared with PCs ($n = 16$) and dendritic-targeting interneurons ($n = 7$). The same key as in Figure 2 is shown. Error bars indicate SEM. *C*, Firing rate plotted against phasic inhibitory charge (Q_i) for individual cells. No significant correlation was found between the firing rate and Q_i in the complete data set (Pearson's correlation). *D*, Firing rate plotted against charge ratio (Q_e/Q_i). A significant positive correlation was found between the firing rate and Q_e/Q_i (Pearson's correlation). A least-square fit line is shown.

Indeed, cell types with high firing rates received, on average, more excitation than cell types with low firing rates (Figs. 2D, 5B).

If inhibition suppresses firing, a negative correlation would be expected between Q_i and the firing rate. This relationship was seen in the reduced data set but failed to reach statistical significance in the full data set (Fig. 5C) (reduced set: $r = -0.40$, $p < 0.05$, $n = 27$; full set: $r = -0.32$, $p = 0.07$, $n = 34$; Pearson's correlation). A stronger correlation was found between the firing rate and Q_e/Q_i (Fig. 5D) (full set: $r = 0.73$, $p < 0.01$, $n = 34$; reduced set: $r = 0.79$, $p < 0.01$, $n = 27$; Pearson's correlation).

Synaptic input and action potential phase-coupling strength
Whereas phase coupling is a robust phenomenon in a large proportion of CA3 neurons, the strength of the phase coupling differed between cells. Could differences in synaptic input account for this variation? We have shown that cell classes differ with respect to the dominant input received from the network (Fig. 2D). Because cell classes also differ in their intrinsic properties, this led to the question of whether cell classes process synaptic input differently. To investigate this, the relationship between Q_e/Q_i and r_{AP} was assessed for each cell type studied. All PCs received a dominant inhibition and showed strong phase coupling. In perisomatic-targeting interneurons, Q_e/Q_i differed between strongly and weakly phase-coupled cells. In this cell group, the dominant input in strongly phase-coupled neurons tended to be excitatory or the inputs were approximately equal such that,
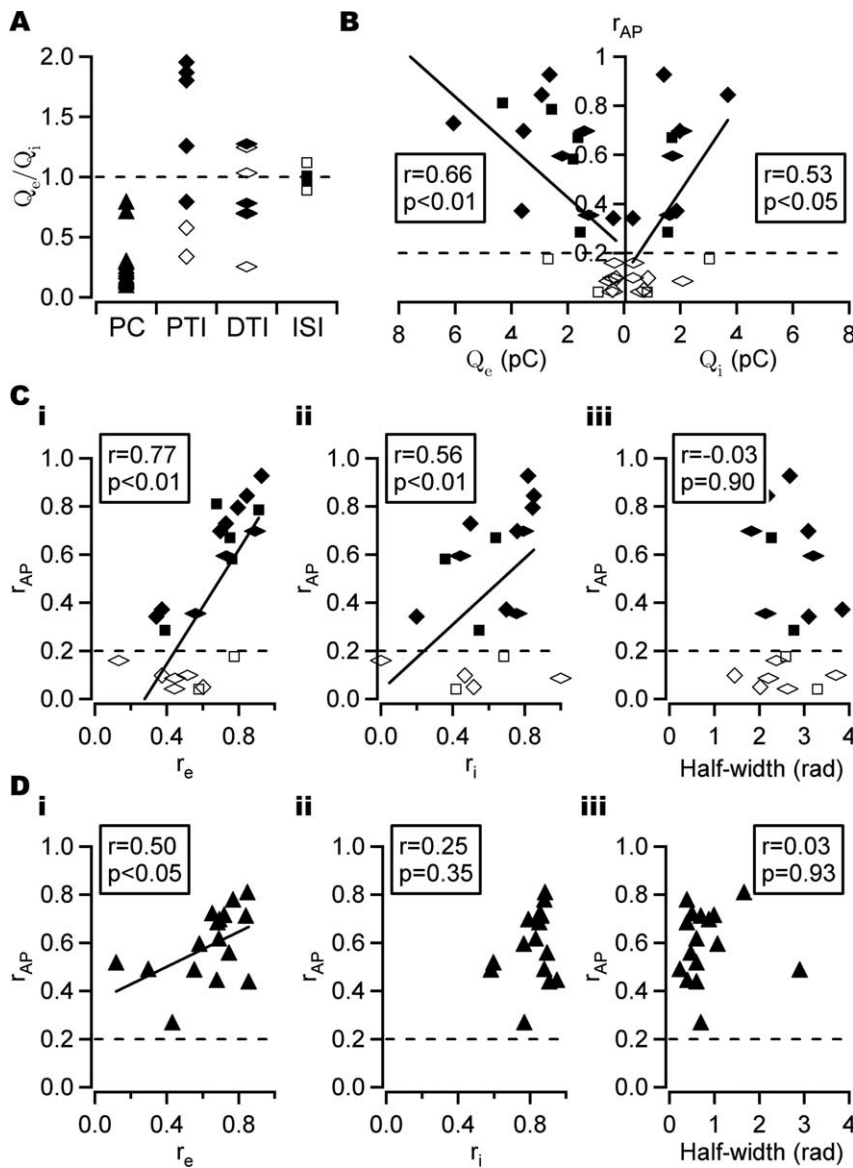
Figure 6. Action potential phase-coupling strength and synaptic input. *A*, Phasic excitatory/inhibitory charge ratio (Q_e/Q_i) in different cell classes. Coupling strength in perisomatic-targeting interneurons differed between strongly and weakly coupled cells, with strongly phase-coupled cells showing, on average, $Q_e/Q_i > 1$, whereas weakly phase-coupled cells received a dominant phasic inhibition ($Q_e/Q_i < 1$). This relationship did not hold for other cell types. The dashed line shows $Q_e/Q_i = 1$. Filled symbols, Strongly phase-coupled cells; open symbols, weakly/non-phase-coupled cells. PTI, Perisomatic-targeting interneuron; DTI, dendritic-targeting interneuron; ISI, interneuron-selective interneuron. The same symbol key applies to all panels. *B*, Action potential phase-coupling strength (r_{AP}) and phasic excitatory charge (Q_e) and phasic inhibitory charge (Q_i) in interneurons. Significant correlations were found between phasic charge transfer and r_{AP} (Pearson's correlation). *C*, r_{AP} and peak EPSC coupling strength (r_e; *i*), peak IPSC coupling strength (r_i; *ii*), and half-width of E_{syn}^{rev} (*iii*) in interneurons. A significant positive correlation was found between r_{AP} and the coupling strength of both EPSC and IPSC peaks. No significant correlation was found between r_{AP} and the half-width of E_{syn}^{rev} (Pearson's correlation). *D*, As in *C*, but in PCs. A correlation was seen between r_{AP} and r_e in PCs, whereas no such correlation was seen for either r_i or the half-width (Pearson's correlation). The dashed line in *B–D* shows $r_{AP} = 0.2$, the cutoff value used to distinguish between strongly and weakly phase-coupled cells. A least-squares fit line is shown for significant correlations.

coupling strength of the cell, it may be that the total synaptic input is more important. Indeed, it was found that strongly phase-coupled perisomatic-targeting interneurons received, on average, a larger synaptic drive (both inhibitory and excitatory) than weakly phase-coupled cells. This result extended to the other interneuron classes studied, in which a significant correlation was found between Q_e and r_{AP} and between Q_i and r_{AP} in the full data set (Fig. 6*B*) (full set: $r = 0.66$, $p < 0.01$, $n = 23$, and $r = 0.53$, $p < 0.05$, $n = 18$, respectively; reduced set: $r = 0.67$, $p < 0.01$, $n = 19$, and $r = 0.3$, $p = 0.27$, $n = 15$, respectively; Pearson's correlation).

If synaptic input controls spike timing, the phase-coupling strength of the synaptic input would be expected to contribute toward the strength of action potential phase coupling. Indeed, in interneurons, a positive correlation was found between r_{AP} and r_e (Fig. 6*Ci*) (full set: $r = 0.77$, $p < 0.01$, $n = 23$; reduced set: $r = 0.73$, $p < 0.01$, $n = 19$; Pearson's correlation), and a weaker correlation was found between r_{AP} and r_i (Fig. 6*Cii*) (full set: $r = 0.56$, $p < 0.01$, $n = 21$; reduced set: $r = 0.47$, $p = 0.057$, $n = 17$; Pearson's correlation), suggesting that it is predominantly the timing precision of excitatory input that controls spike-timing precision in interneurons. In PCs, the correlation between r_{AP} and r_e was weaker than in interneurons (Fig. 6*Di*) (full set: $r = 0.50$, $p < 0.05$, $n = 16$; reduced set: $r = 0.37$, $p = 0.23$, $n = 12$; Pearson's correlation), whereas no significant correlation was found between r_{AP} and r_i (Fig. 6*Dii*) (full set: $r = 0.25$, $p = 0.35$, $n = 16$; reduced set: $r = 0.14$, $p = 0.66$, $n = 12$; Pearson's correlation).

Because cells receive excitatory and inhibitory inputs concomitantly, the temporal interaction of excitation and inhibition may also contribute toward the action potential coupling strength. If the net resultant synaptic input alone controls spike time, then the width of the peak of E_{syn}^{rev} should give a time window for action potential firing. A correlation analysis of the half-width of E_{syn}^{rev} and r_{AP} revealed no such relationship in interneurons (Fig. 6*Ciii*) (full set: $r = -0.03$, $p = 0.90$, $n = 18$; reduced set: $r = -0.29$, $p = 0.30$, $n = 15$; Pearson's correlation) or PCs (Fig. 6*Diii*) (full set: $r = 0.03$, $p = 0.93$, $n = 16$; reduced set: $r = 0.03$, $p = 0.93$, $n = 12$; Pearson's correlation).

We conclude that both the precision and strength of synaptic input contribute toward controlling r_{AP} in interneurons.

Synaptic input and mean action potential phase angle
We have shown that different classes of cell preferentially fire at different phases of the gamma oscillation. Could differences in

on average, $Q_e/Q_i > 1$, whereas weakly phase-coupled cells received a dominant inhibitory input ($Q_e/Q_i < 1$). This relationship was not observed in other cell types. Dendritic-targeting interneurons showed a broad range of Q_e/Q_i and variable r_{AP}, whereas the ratio of excitation to inhibition in interneuron-selective interneurons was approximately equal, with Q_e/Q_i values closer to 1 independent of the value of r_{AP} (Fig. 6*A*).

If the ratio of excitation to inhibition cannot fully explain the

the timing of the synaptic input account for the differences in mean action potential phase angle? The relationship between ϕ_{AP} and synaptic input was investigated next. ϕ_{AP} in strongly phase-coupled cells was found to either follow (10 of 26) or precede (16 of 26) the peak of the cycle-averaged EPSC and always preceded the peak of the cycle-averaged IPSC (Fig. 7A). When the effects of excitation and inhibition were combined through the estimation of E_{syn}^{rev}, it was found that the peak of E_{syn}^{rev} (ϕ_{syn}) preceded ϕ_{AP} in the vast majority of strongly phase-coupled cells (24 of 26). In PCs, ϕ_{syn} reflected the phase of least inhibition, whereas in phase-coupled perisomatic-targeting interneurons and other interneurons receiving a large excitatory input, it was associated with the peak of the excitation (Fig. 7B).

If the timing of excitatory input controls spike timing in all cells, it might be expected that excitation arrives earlier in PCs than in interneurons, because they fire at earlier phases. However, the phase of peak excitation was significantly later in phase-coupled PCs ($\phi_E = -1.1 \pm 0.08$; $n = 16$) than in phase-coupled interneurons (Fig. 7C) (full set: $p < 0.01$; perisomatic-targeting interneurons: $\phi_E = -1.8 \pm 0.25$, $n = 7$; dendritic-targeting interneurons: $\phi_E = -1.7 \pm 0.04$, $n = 3$; interneuron-selective interneurons: $\phi_E = -1.5 \pm 0.15$, $n = 5$; reduced set: $p < 0.01$, Watson-Williams test; $n = 26$). This suggests that it is not excitation alone that governs precise action potential timing. Indeed, when the effect of excitation and inhibition were combined, ϕ_{syn} was found to be significantly earlier in phase-coupled PCs ($\phi_{syn} = -2.7 \pm 0.09$; $n = 16$) than in phase-coupled interneurons (Fig. 7D) (full set: $p < 0.01$; perisomatic-targeting interneurons: $\phi_{syn} = -2.2 \pm 0.20$, $n = 5$; dendritic-targeting interneurons: $\phi_{syn} = -1.7 \pm 0.05$, $n = 3$; interneuron-selective interneurons: $\phi_{syn} = -2.1 \pm 0.86$, $n = 2$; reduced set: $p < 0.01$, Watson-Williams test; $n = 20$), resulting in a significant correlation between ϕ_{syn} and ϕ_{AP} over all cells (Fig. 7E) (full set: $r = 0.46$, $p < 0.01$, $n = 26$; reduced set: $r = 0.61$, $p < 0.01$, $n = 20$; angular–angular correlation).

In conclusion, we have shown that differences in synaptic input are important in controlling the distinct firing properties of neurons during gamma oscillations.

Figure 7. Mean action potential phase and synaptic input in strongly phase-coupled cells. *A*, Cycle-averaged EPSC (solid trace) and IPSC (dashed trace) with a mean firing phase (ϕ_{AP}) shown as a dotted line in a PC (*i*) and perisomatic-targeting interneuron (*ii*). ϕ_{AP} either slightly led or lagged the (negative) peak of the cycle-averaged EPSC but was always earlier than the (positive) peak of cycle-averaged IPSC in phase-coupled cells. *B*, E_{syn}^{rev} (solid line) and spike-phase histogram (gray) for the same cells as shown in *A*. The peak of E_{syn}^{rev} (ϕ_{syn}; dashed-dotted line) preceded ϕ_{AP} in the majority of phase-coupled cells. Note that ϕ_{AP} does not necessarily coincide with the peak of the spike-phase histogram. *C*, Phase of peak excitation (ϕ_e) in different cell types. The phase of peak excitation arrived significantly later in PCs than in perisomatic-targeting interneurons, dendritic-targeting interneurons, and interneuron-selective interneurons. *D*, ϕ_{syn} in different cell types. ϕ_{syn} occurred significantly earlier in PCs than in perisomatic-targeting interneurons and dendritic-targeting interneurons. *E*, ϕ_{AP} and ϕ_{syn} plotted for individual strongly phase-coupled cells. A significant positive correlation was found (angular–angular correlation). A least-squares fit line is shown. The same key as in *C* and *D* is used. *$p < 0.05$; **$p < 0.01$. PTI, Perisomatic-targeting interneuron; DTI, dendritic-targeting interneuron; ISI, interneuron-selective interneuron.

Discussion
It has been reported previously that different subclasses of CA3 neurons differ in their firing properties during cholinergically induced oscillations (McMahon et al., 1998; Hájos et al., 2004).
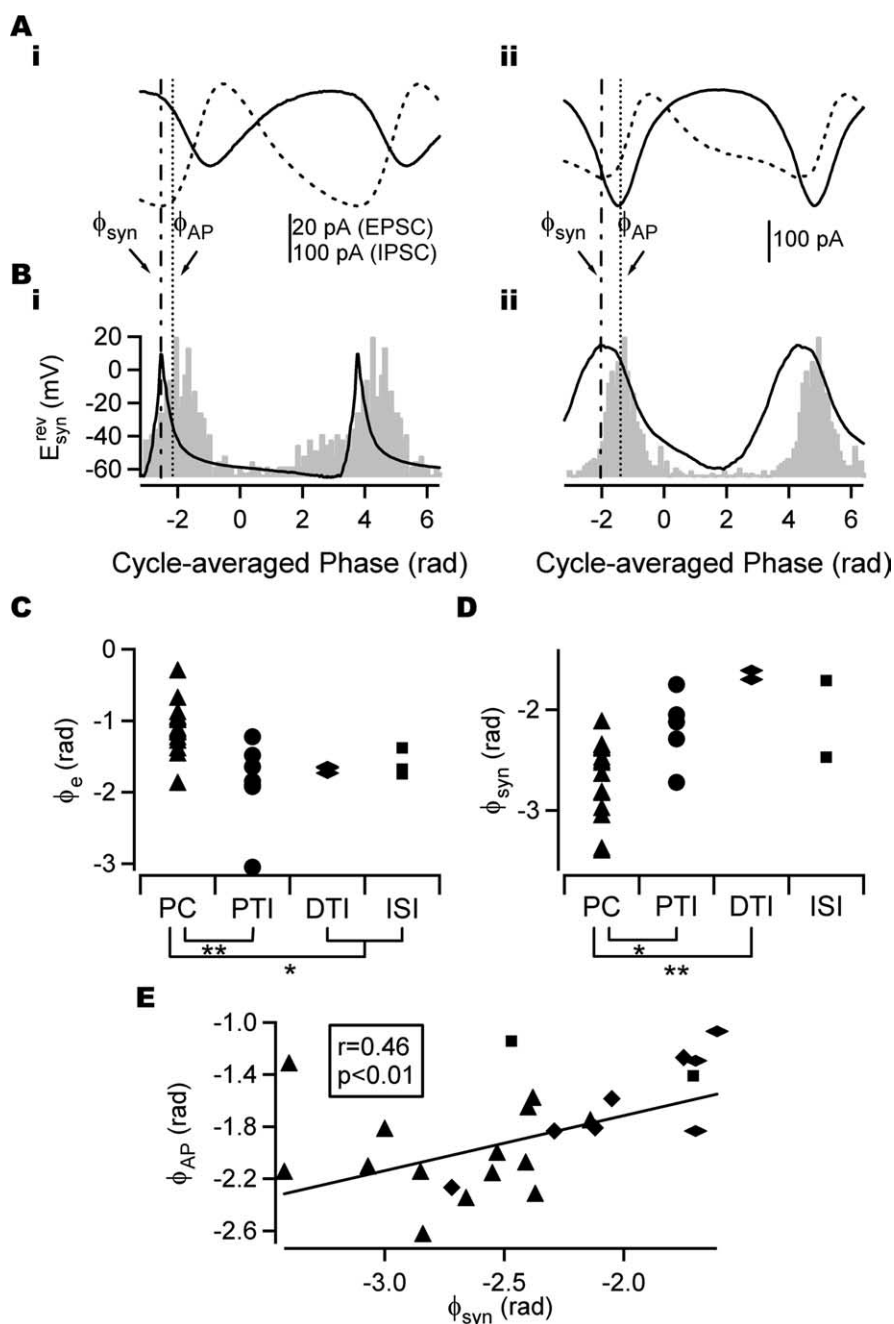
The present study investigated PSCs in anatomically identified CA3 neurons during CCh-induced network oscillations and related the PSCs to the firing properties of the cells. Our main findings were as follows: (1) synaptic input differed between cell classes during cholinergically induced gamma oscillation; and (2)

features of synaptic input could be used to predict firing properties, namely firing rate and spike timing (quantified by phase-coupling strength and mean phase angle).

Variability in CCh-induced field oscillation

Wavelet analysis revealed a rhythmicity in the magnitude of the field oscillation in approximately half of the recordings. This could arise from the interference of oscillators, oscillating at similar, but unequal frequencies, or, alternatively, from slow membrane potential oscillations. Cunningham et al. (2003) suggested that I_h-dependent membrane potential oscillations of stellate cells can produce a theta-frequency modulation of gamma oscillations in the entorhinal cortex. Theta-frequency membrane potential oscillations have been recorded in hippocampal PCs (Leung and Yim, 1991), raising the possibility that a similar mechanism may generate the low frequency modulation seen here. These possibilities were not explored further.

Different synaptic input in distinct cell classes and local network architecture

Cell classes differed in their dominant synaptic input. Inhibitory synaptic currents exceeded excitatory synaptic currents in all PCs, whereas excitation was, on average, stronger and often dominated over inhibition in phase-coupled perisomatic-targeting interneurons. In fact, these phase-coupled neurons received the largest excitatory input of all cell types. In line with these results, anatomical investigations have revealed that perisomatic-targeting interneurons containing the calcium binding protein parvalbumin received the largest number of excitatory synapses among all inhibitory cells (Gulyas et al., 1999).

Based on current source density analysis and spike-time measurement, it has been suggested that hippocampal gamma oscillations arise from the disynaptic interaction of excitatory PCs and inhibitory perisomatic-targeting interneurons (Mann et al., 2005a,b). Our data provide the first direct evidence of the synaptic currents in these neuronal populations (Fig. 2) and is consistent with a recurrent inhibitory model of gamma oscillations (Freeman, 1968). This model is supported by four of our findings: (1) the relative spike times of PCs and interneurons (Fig. 4); (2) the relative timing of excitatory and inhibitory events (Fig. 3B); (3) the differences in excitatory and inhibitory charge in different cell types (Fig. 2); and (4) the differences in coupling strength of the IPSC peak in different cell types. The fact that r_i was larger in PCs than in interneurons (Fig. 3A) is in agreement with a recurrent model of gamma oscillogenesis in which a strongly phase-coupled interneuron population provides a perisomatic source of inhibition to PCs, whereas interneurons receive inhibition from numerous subpopulations of interneurons with varied phase coupling. Interestingly, Mann et al. (2005b) observed that the current source was not confined to the soma and axon initial segment but extended to the proximal dendritic region. In our sample, we have recorded from two inhibitory neurons that arborize in the proximal dendritic region (data not included), that showed phase coupling, and received a large excitatory current, comparable to perisomatic-targeting interneurons, suggesting that this population might also be actively involved in oscillogenesis.

Synaptic input controls spike output

Although differences in synaptic input exist between cell classes, it appears that the cell classes also differ in their responses to similar synaptic input (Fig. 6A). This raises the question of the importance of synaptic input versus the intrinsic properties of a cell in the control of firing properties during gamma oscillations.

Firing rate
It was found that PCs fire at a significantly lower rate than interneurons. Although intrinsic conductances, such as the one underlying I_h, can contribute to setting a firing rate preference (Maccaferri and McBain, 1996; Pike et al., 2000, Hu et al., 2002), differences in synaptic input could also account for differences in the firing rate. Indeed, over all cells, a stronger positive correlation was found between the firing rate and Q_e/Q_i than between the firing rate and Q_e, suggesting that both phasic excitation and inhibition contribute toward controlling the firing rate. Furthermore, cell types with high firing rates received larger phasic excitatory synaptic input than cell types with lower firing rates, supporting the conclusion that although intrinsic properties set a firing rate preference, synaptic input also clearly contributes to the differences in firing rates of different cell types.

Spike-timing precision
The ability of neurons to fire action potentials reliably and precisely has been shown for artificially generated input (Mainen and Sejnowski, 1995; Hunter et al., 1998; Fellous et al., 2001; Haas and White, 2002). The CCh model allows for a measure of precision under more physiological conditions. A precise spike output could be the result of intrinsic membrane properties, net synaptic input, or an interaction between the two. The SD of the spike phase distribution was smaller than the equivalent measure for absolute spike time in strongly phase-coupled cells. The opposite relationship was seen in weakly phase-coupled cells. This suggests that synaptic input provides a considerable contribution to the control of spike timing in strongly phase-coupled neurons.

Action potential phase-coupling strength
We found that all interneuron types, including dendritic-targeting interneurons, fire phase coupled to the oscillation when they receive sufficiently strong excitatory synaptic input (Fig. 6B). Moreover, perisomatic-targeting interneurons receiving a dominant excitation were strongly phase coupled, whereas those with $Q_e/Q_i < 1$ tended not to be. However, the relationship of Q_e/Q_i to r_{AP} seen in perisomatic-targeting interneurons was not observed in other cell types. The apparent lack of relationship between phasic charge ratio and r_{AP} in dendritic-targeting and interneuron-selective interneurons could be attributable to the relatively small number of neurons sampled, or to the fact that these cells were treated as two populations when, in fact, they are composed of several distinct subpopulations (radiatum and OLM, and IS-1, IS-2, and IS-3, respectively) (Freund and Buzsaki, 1996). Differences in intrinsic properties might also contribute toward the observed differences between cell types in the relationship between Q_e/Q_i and r_{AP}.

In interneurons, a positive correlation was found between the phase-coupling strength of synaptic current and action potentials, suggesting that a more precise input leads to a more precise output. Moreover, the correlation was stronger for excitatory inputs, corroborating the conclusion that interneuron spike phase precision is primarily controlled by PCs. In PCs, no strong correlation was found between the precision of the peak phase of synaptic input and r_{AP}, suggesting that other factors control the precise time of action potential generation in this cell class.

If the net synaptic input sets the time window for action potential firing, and because PCs had a narrow E_{syn}^{rev} peak compared with interneurons, it might be expected that the coupling of PC firing to the oscillation be stronger than interneuron phase coupling, because PCs had a narrow E_{syn}^{rev} peak compared with interneurons. However, this was not the case, because phase coupling of PCs was weaker than that of phase-coupled interneurons, in

line with previous findings (Hájos et al., 2004). Consistent with these findings, Fricker and Miles (2000) demonstrated that most CA1 interneurons fire more precisely in response to excitatory input than do PCs. They attributed this difference to differences in intrinsic properties between these cell types. Similarly, differences in intrinsic properties, as well as differences in the somato-dendritic distribution of synaptic inputs, might account for some of the differences in spike phase precision observed here. Future experiments will be needed to dissociate the relative contributions of synaptic input and intrinsic properties toward spike output.

Mean action potential phase angle

Action potentials occurred, on average, earlier in PCs than in interneurons, yet the peak of synaptic excitation occurred later in PCs. However, ϕ_{syn}, which approximates the time when phasic excitation is most dominant relative to phasic inhibition, occurred significantly earlier in PCs than in interneurons, suggesting that both excitation and inhibition are important in the control of spike timing. In PCs, ϕ_{syn} occurred when inhibition is at a minimum, whereas in perisomatic-targeting interneurons, the main target of PCs, ϕ_{syn} occurred near the peak of the excitation. Hence, during gamma oscillations, PC spike time is controlled by inhibition, whereas excitation is important in the control of perisomatic-targeting interneuron spike timing. It has been reported, however, that the average firing rate of PCs *in vivo* is significantly lower than that observed here (Csicsvari et al., 2003). Thus, even with a higher recurrent connectivity in the intact brain, Q_e might be overestimated in our study, and PC control of perisomatic-targeting interneuron spike timing may be complemented by other mechanisms *in vivo*, such as interneuronal gap junctions (Traub et al., 2001).

In conclusion, our findings support a model of cholinergically induced gamma oscillations mediated by an interaction of PCs and perisomatic-targeting interneurons. The results highlight the importance of synaptic input in the control of firing in both PCs and interneurons. These results shed light on the mechanism underlying hippocampal gamma oscillations *in vitro*. A thorough understanding of the mechanism of *in vitro* oscillogenesis may provide a first step toward understanding the mechanism and function of these oscillations in the intact brain.

References

Amaral DG, Ishizuka N, Claiborne B (1990) Neurons, numbers and the hippocampal network. Prog Brain Res 83:1–11.

Bacci A, Huguenard JR (2006) Enhancement of spike-timing precision by autaptic transmission in neocortical inhibitory interneurons. Neuron 49:119–130.

Bragin A, Jando G, Nadasdy Z, Hetke J, Wise K, Buzsaki G (1995) Gamma (40–100 Hz) oscillation in the hippocampus of the behaving rat. J Neurosci 15:47–60.

Buzsaki G, Leung LW, Vanderwolf CH (1983) Cellular bases of hippocampal EEG in the behaving rat. Brain Res 287:139–171.

Csicsvari J, Jamieson B, Wise KD, Buzsaki G (2003) Mechanisms of gamma oscillations in the hippocampus of the behaving rat. Neuron 37:311–322.

Cunningham MO, Davies CH, Buhl EH, Kopell N, Whittington MA (2003) Gamma oscillations induced by kainate receptor activation in the entorhinal cortex *in vitro*. J Neurosci 23:9761–9769.

Fellous JM, Houweling AR, Modi RH, Rao RP, Tiesinga PH, Sejnowski TJ (2001) Frequency dependence of spike timing reliability in cortical pyramidal cells and interneurons. J Neurophysiol 85:1782–1787.

Fisahn A, Pike FG, Buhl EH, Paulsen O (1998) Cholinergic induction of network oscillations at 40 Hz in the hippocampus in vitro. Nature 394:186–189.

Fisher NI (1993) Statistical analysis of circular data. Cambridge, UK: Cambridge UP.

Freeman WJ (1968) Relations between unit activity and evoked potentials in prepyriform cortex of cats. J Neurophysiol 31:337–348.

Freund TF, Buzsaki G (1996) Interneurons of the hippocampus. Hippocampus 6:347–470.

Fricker D, Miles R (2000) EPSP amplification and the precision of spike timing in hippocampal neurons. Neuron 28:559–569.

Gloveli T, Dugladze T, Saha S, Monyer H, Heinemann U, Traub RD, Whittington MA, Buhl EH (2005a) Differential involvement of oriens/pyramidale interneurones in hippocampal network oscillations *in vitro*. J Physiol (Lond) 562:131–147.

Gloveli T, Dugladze T, Rotstein HG, Traub RD, Monyer H, Heinemann U, Whittington MA, Kopell NJ (2005b) Orthogonal arrangement of rhythm-generating microcircuits in the hippocampus. Proc Natl Acad Sci USA 102:13295–13300.

Gulyas AI, Megias M, Emri Z, Freund TF (1999) Total number and ratio of excitatory and inhibitory synapses converging onto single interneurons of different types in the CA1 area of the rat hippocampus. J Neurosci 19:10082–10097.

Haas JS, White JA (2002) Frequency selectivity of layer II stellate cells in the medial entorhinal cortex. J Neurophysiol 88:2422–2429.

Hájos N, Pálhalmi J, Mann EO, Nemeth B, Paulsen O, Freund TF (2004) Spike timing of distinct types of GABAergic interneuron during hippocampal gamma oscillations *in vitro*. J Neurosci 24:9127–9137.

Hu H, Vervaeke K, Storm JF (2002) Two forms of electrical resonance at theta frequencies, generated by M-current, h-current and persistent Na+ current in rat hippocampal pyramidal cells. J Physiol (Lond) 545:783–805.

Hunter JD, Milton JG, Thomas PJ, Cowan JD (1998) Resonance effect for neural spike time reliability. J Neurophysiol 80:1427–1438.

Leung LW, Yim CY (1991) Intrinsic membrane potential oscillations in hippocampal neurons *in vitro*. Brain Res 553:261–274.

Le Van Quyen M, Foucher J, Lachaux J, Rodriguez E, Lutz A, Martinerie J, Varela FJ (2001) Comparison of Hilbert transform and wavelet methods for the analysis of neuronal synchrony. J Neurosci Methods 111:83–98.

Maccaferri G, McBain CJ (1996) The hyperpolarization-activated current (Ih) and its contribution to pacemaker activity in rat CA1 hippocampal stratum oriens-alveus interneurones. J Physiol (Lond) 497:119–130.

Mainen ZF, Sejnowski TJ (1995) Reliability of spike timing in neocortical neurons. Science 268:1503–1506.

Mann EO, Radcliffe CA, Paulsen O (2005a) Hippocampal gamma-frequency oscillations: from interneurones to pyramidal cells, and back. J Physiol (Lond) 562:55–63.

Mann EO, Suckling JM, Hájos N, Greenfield SA, Paulsen O (2005b) Perisomatic feedback inhibition underlies cholinergically induced fast network oscillations in the rat hippocampus *in vitro*. Neuron 45:105–117.

McMahon LL, Williams JH, Kauer JA (1998) Functionally distinct groups of interneurons identified during rhythmic carbachol oscillations in hippocampus *in vitro*. J Neurosci 18:5640–5651.

Paulsen O, Sejnowski TJ (2006) From invertebrate olfaction to human cognition: emergent computational functions of synchronized oscillatory activity. J Neurosci 26:1661–1662.

Penttonen M, Kamondi A, Acsady L, Buzsaki G (1998) Gamma frequency oscillation in the hippocampus of the rat: intracellular analysis *in vivo*. Eur J Neurosci 10:718–728.

Pike FG, Goddard RS, Suckling JM, Ganter P, Kasthuri N, Paulsen O (2000) Distinct frequency preferences of different types of rat hippocampal neurones in response to oscillatory input currents. J Physiol (Lond) 529:205–213.

Stewart M, Fox SE (1990) Do septal neurons pace the hippocampal theta rhythm? Trends Neurosci 13:163–168.

Torrence C, Compo GP (1998) A practical guide to wavelet analysis. Bull Am Meteorol Soc 79:61–78.

Traub RD, Kopell N, Bibbig A, Buhl EH, LeBeau FE, Whittington MA (2001) Gap junctions between interneuron dendrites can enhance synchrony of gamma oscillations in distributed networks. J Neurosci 21:9478–9486.

Vida I, Bartos M, Jonas P (2006) Shunting inhibition improves robustness of gamma oscillations in hippocampal interneuron networks by homogenizing firing rates. Neuron 49:107–117.

Whittington MA, Traub RD (2003) Interneuron diversity series: inhibitory interneurons and network oscillations *in vitro*. Trends Neurosci 26:676–682.

Whittington MA, Traub RD, Jefferys JG (1995) Synchronized oscillations in interneuron networks driven by metabotropic glutamate receptor activation. Nature 373:612–615.

Zar JH (1999) Biostatistical analysis. Upper Saddle River, NJ: Prentice Hall.